

RESEARCH

Open Access



ZnO-Cu/Mn nanozyme for rescuing the intestinal homeostasis in *Salmonella*-induced colitis

Aimin Wu^{1†}, Chen Liang^{2†}, WenShuang Chen², ChangFang Lu², JunZhou Chen¹, Bing Wu³, Daiwen Chen^{1*}, Li He^{2*} and Xianxiang Wang^{2*}

Abstract

Salmonella is one of the most common foodborne pathogens, which can cause severe enteritis and intestinal microbiota imbalance. However, there are limited strategies currently available for preventing or treating *Salmonella*-induced colitis. Herein, we developed the Cu/Mn-co-doped ZnO tandem nanozyme (ZnO-CM) with pH-responsive multienzyme-mimicking activities via doping engineering for the treatment of *Salmonella*-induced colitis. Benefiting from the co-doping of Cu and Mn, ZnO-CM nanospheres exhibit remarkable peroxidase-like activity in acidic condition and superoxide dismutase- and catalase-like activities in neutral environment. Animal experiments show that ZnO-CM can efficiently inhibit bacterial growth, alleviate inflammation, and restore the intestinal barrier, resulting in good antibacterial and anti-inflammatory effects on *Salmonella*-induced colitis. Mechanistically, ZnO-CM functions through inhibiting the continuous accumulation of ROS, increasing the levels of tight junction proteins occludin and claudin-1, and decreasing the expression of pro-inflammatory cytokines IL-1 β and IL-6 in intestine. This work not only presents an effective paradigm for *Salmonella*-induced colitis therapy, but also provides new sights into the prevention and treatment of other bacterial enteritis.

Keywords ZnO-CM nanozymes, pH-responsive, *Salmonella*, Oxidative stress, Bacterial enteritis

Introduction

Salmonella is a major foodborne pathogen that can cause severe intestinal microbiota imbalance, enteritis, and sepsis, leading to an estimated 108.1 million gastroenteritis cases and 291,000 deaths annually worldwide [1, 2, 3]. It colonizes the intestinal lumen, survives in host tissues, and breaches the intestinal epithelial barrier to enter the bloodstream, complicating treatment with traditional antibiotics [4, 5, 6]. The intestinal epithelial barrier is crucial for preventing pathogens and toxins from entering the bloodstream [7, 8], but *Salmonella* can circumvent this defense, triggering the oxidative stress and inflammation [9, 10], which can lead to systemic infections [11]. This property poses a certain difficulty for treatment, especially for traditional antibiotics that can't

[†]Aimin Wu and Chen Liang contributed equally to this work.

*Correspondence:

Daiwen Chen
chendwz@sicau.edu.cn

Li He
lihe@sicau.edu.cn

Xianxiang Wang
xianxiangwang@hotmail.com

¹Institute of Animal Nutrition, Sichuan Agricultural University, Chengdu 611130, China

²College of Science, Sichuan Agricultural University, Chengdu 611130, Sichuan, China

³Sichuan Chelota Biotechnology Group Co., Ltd, Chengdu 618302, Sichuan, China



penetrate the cell effectively or have no selective effect on endotoxins [12]. Therefore, the development of new therapies for intracellular pathogens is crucial. ZnO has been extensively studied as a cost-effective and widely utilized antimicrobial agent. Additionally, it is classified as a Generally Recognized As Safe (GRAS) material by the U.S. Food and Drug Administration (21 CFR 182.8991) [13]. However, its effectiveness against *Salmonella* often necessitates high concentrations, making it challenging to achieve efficient sterilization both intracellularly and extracellularly. Enhancing the bactericidal efficacy of ZnO is critical for the control and treatment of *Salmonella* infections. Nanozymes are nanomaterials with enzyme-like properties that exhibit exceptional stability under harsh environmental conditions. They effectively eliminate free radicals and prevent the oxidative stress, showcasing significant antimicrobial activity [14, 15, 16].

In antioxidant defense, trace elements such as copper (Cu), manganese (Mn), and zinc (Zn) act as cofactors for various enzymes [17]. Cu and Mn ions help catalyze the conversion of harmful superoxide radicals into less active molecules, which is a key step in the cellular defense mechanism [18]. Although Zn does not directly participate in the neutralization of free radicals, it is crucial for the structural stability and correct folding of enzymes [19], thereby ensuring their catalytic activity. In this study, we explore the doping trace amounts of Cu and Mn into the antimicrobial material ZnO, which itself does not possess antioxidant enzyme activity. This modification not only enhances the original antibacterial

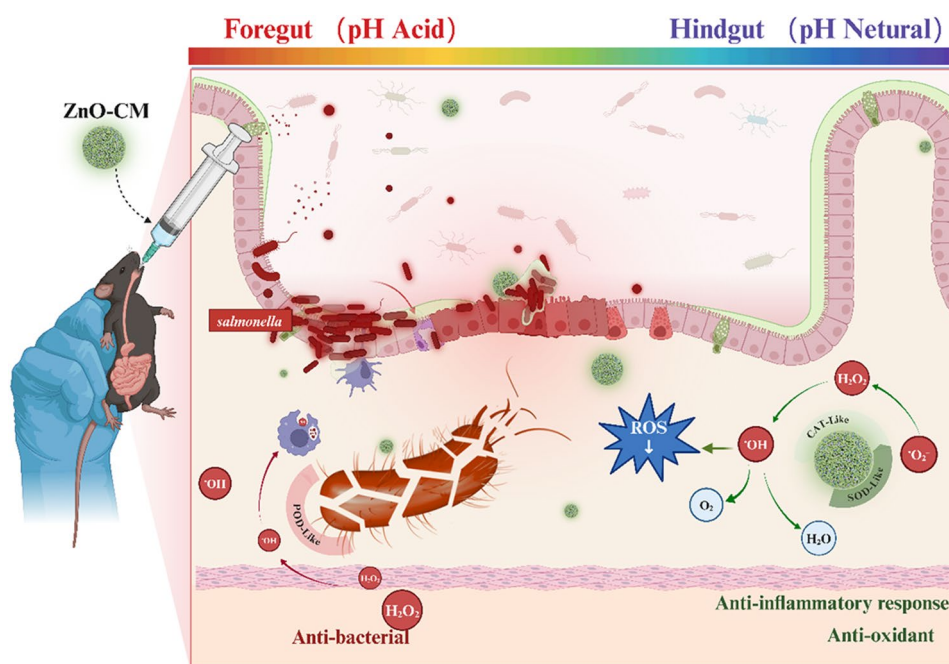
effect of ZnO but also mimics the enzymatic activities of major antioxidant defenses, such as superoxide dismutase (SOD), catalase (CAT) and peroxidase (POD). This Cu/Mn-co-doped ZnO tandem nanozyme (ZnO-CM) exhibits POD activity in the upper gastrointestinal tract (acidic environment), inducing hydroxyl radicals (OH) generation, thus killing *Salmonella*. Interestingly, in the hindgut (neutral or alkaline environment), ZnO-CM nanozyme exhibits SOD and CAT activity, reducing the generation of reactive oxygen species (ROS) [20], and reducing systemic inflammation induced by *Salmonella* infection. These actions reshape the colitis environment, alleviate intestinal damage caused by *Salmonella* infection, and ultimately improve intestinal homeostasis and health [21, 22]. Therefore, this research not only provides a safe and reliable strategy for preventing and treating *Salmonella*-induced colitis but also offers new insights into the prevention and control of other bacterial enteritis and antibiotic-resistant bacterial infections. (Scheme 11)

Methods

Materials and instruments

Oleylamine (OAm) was sourced from Macklin, while zinc chloride heptahydrate (ZnCl_2 , AR,99%), copper chloride dihydrate ($\text{CuCl}_2 \cdot 2\text{H}_2\text{O}$, AR,99%), and manganese chloride tetrahydrate ($\text{MnCl}_2 \cdot 4\text{H}_2\text{O}$, AR,99%) were acquired from KESHI.

The ZnO-CM material underwent comprehensive characterization, employing various techniques.



Scheme 1 Schematic representation of the antibacterial and anti-inflammatory activities of ZnO-CM against *Salmonella*-induced colitis. (Created with Biorender)

Scanning electron microscopy (SEM, Hitachi SU-8010) and transmission electron microscopy (TEM, JEOL-2100 F) were utilized for imaging. Elemental analysis was performed using energy-dispersive spectrometry (EDS, Hitachi SU-8100) and inductively coupled plasma mass spectrometry (ICP-MS-7700). The crystalline structure of ZnO-CM was assessed through X-ray powder diffraction (XRD, D8 Advance), while X-ray photoelectron spectroscopy (XPS) measurements were carried out using the Escalab 250xi instrument. Zeta potential was measured with the NANO ZS instrument, and the generation of oxygen vacancies and hydroxyl radicals under acidic conditions was verified through electron paramagnetic resonance (EPR, Bruker A300) analysis.

Synthesis of ZnO, ZnO-Cu, ZnO-Mn, and ZnO-CM

ZnO-CM nanospheres were synthesized using a simple hydrothermal method. In brief, 1.6358 g of zinc chloride was added to 120 mL of anhydrous ethanol (100 mM) and refluxing at 80 °C for 30 min under magnetic stirring. After 1 mL of oleylamine was added and stirred for 1 h at normal temperature, 10% molar mass of copper chloride and 5% molar mass of manganese chloride were added and stirred for 30 min. After screening, this ratio can achieve the best antibacterial effect with the least doping amount. (Fig.S1) Subsequently, the mixture was transferred into a polytetrafluoroethylene autoclave and heated at 200 °C for 3 h. The resulting products were collected by centrifugation at 4200 rpm for 10 min, and then washed three times with ethanol. Finally, the products were dried in a vacuum oven at 60 °C for 24 h. The synthesis of ZnO, ZnO-Cu, and ZnO-Mn closely followed the procedure used for ZnO-CM, with the distinction that no copper or manganese was added in the case of ZnO, and only a single element (either copper or manganese) was included for the corresponding composites.

Enzyme activity assay

Colorless 3,3,5,5-tetramethylbenzidine (TMB), which can be oxidized to blue product (oxTMB) exhibiting a characteristic UV-visible absorption peak at 652 nm, was employed as the indicator. A 0.1 M acetic acid buffer (pH 3–8) was utilized to adjust the total volume of the reaction system to 3 mL. In this mixed system, the absorbance of the oxidized TMB product increased over time. The formation of the complex was monitored by UV-visible spectroscopy, recording changes in absorbance at 652 nm, which indirectly indicated the peroxidase-like activity of the ZnO-CM nanozyme.

The nitroblue tetrazolium (NBT) colorimetric method was employed to assess the activity of superoxide dismutase (SOD). In this method, superoxide anions (O_2^-) are generated through the reaction of xanthine and xanthine oxidase (XO), resulting in the reduction of NBT to

formazan, a blue-violet compound that exhibits strong absorption at 560 nm. SOD competes with this process by eliminating superoxide anions, thereby inhibiting formazan formation. Consequently, a more intense blue-violet color in the reaction mixture indicates lower SOD activity, while a lighter color suggests higher enzyme activity. This relationship allows for quantitative assessment of SOD activity through colorimetric analysis. The activity of catalase (CAT) in decomposing H_2O_2 can be measured using the ammonium molybdate method. In this approach, the reaction between CAT and H_2O_2 is promptly halted by the addition of ammonium molybdate. Any remaining H_2O_2 subsequently reacts with ammonium molybdate to form a pale-yellow complex. The change in concentration of this complex, measured at 405 nm, provides a basis for calculating CAT activity.

Electron paramagnetic resonance spectrometer (ESR) measurements

The ZnO, ZnO-Cu, ZnO-Mn and ZnO-CM nanoparticles were dispersed in an HAc-NaAc (0.1 mol/L, pH 3) solution for the hydroxyl radical tests. The trapping agent utilized in this test was 5,5-dimethyl-1-pyrroline-N-oxide (DMPO). The trapping agent was pipetted into the solution and mixed homogeneously for preparation, and then, capillaries were introduced to load the samples. Then, the capillaries were placed into an electron paramagnetic resonance machine (Bruker, A300) to collect information about the radicals.

Calculation of enzyme activity

All calculations were conducted using density functional theory (DFT) as implemented in the Vienna Ab Initio Simulation Package (VASP). The exchange-correlation potential was described using the generalized gradient approximation of Perdew-Burke-Ernzerhof (GGA-PBE). Interactions between ion cores and valence electrons were treated using the projector augmented-wave (PAW) method. The plane-wave cutoff energy was set to 400 eV. Structural models were optimized until the Hellmann-Feynman forces were less than -0.02 eV/Å and the change in energy was below 10^{-5} eV. Long-range van der Waals interactions were accounted for using the DFT-D3 approach. The Gibbs free energy change is defined as follows:

$$\Delta G = \Delta E + \Delta ZPE - T\Delta S$$

where ΔE represents the electronic energy calculated using VASP, ΔZPE denotes the difference in zero-point energy, and ΔS indicates the entropy change between the products and reactants. The temperature (T) is set at 298.15 K.

Antimicrobial performance assay *in vitro*

Take the *Salmonella* (*Salmonella enterica* serovar *Typhimurium*, ST, ATCC14028) strain from the -80°C freezer and thaw it in water at 37°C until it is reactivated. Inoculate $10\ \mu\text{L}$ of the bacterial solution into $10\ \text{mL}$ of LB broth (inoculation volume 0.1%) and incubate in a shaking incubator at 37°C for 12 h. Then inoculate $1\ \text{mL}$ of the activated bacteria into $9\ \text{mL}$ of medium and continue to incubate in a shaking incubator at 37°C until the OD (600 nm) reaches 0.5, after which dilute it by 10^5 times. Add $100\ \mu\text{L}$ of bacterial suspension ($1 \times 10^6\ \text{CFU}/\text{mL}$) + $100\ \mu\text{L}$ of PBS (blank control group), and $100\ \mu\text{L}$ of bacterial suspension + $100\ \mu\text{L}$ of materials (30–2000 $\mu\text{g}/\text{mL}$ ZnO-CM, ZnO, ZnO-Cu, ZnO-Mn experimental groups, with samples diluted in a 2-fold gradient) into a 96-well plate and incubate for 2 h. Then, spread $100\ \mu\text{L}$ of the bacterial suspension onto LB agar plates and spread evenly. After inverting and incubating at 37°C in a constant temperature incubator for 12 h. Finally, record the CFU. A $10\ \text{mL}$ bacterial suspension (ST) was added to sterile conical flasks, followed by the addition of ZnO, ZnO-Cu, ZnO-Mn, and ZnO-CM to achieve a final concentration of $60\ \mu\text{g}/\text{mL}$. The cultures were incubated at 37°C in a rotary shaker set to 220 rpm. Optical density at 600 nm (OD600) was measured at intervals of 0, 2, 4, 6, 8, 10, 12, 14, 16, 18, 20, and 24 h to construct the growth curve. Additionally, ST was treated with a $30\ \mu\text{g}/\text{mL}$ ZnO solution, incubated for 2 h at 37°C and 200 rpm, then centrifuged at 3000 rpm for 5 minutes. The supernatant was removed, and $1\ \text{mL}$ of 2.5% glutaraldehyde solution was added for fixation. The microstructures of ST were characterized using SEM and TEM.

Protein leakage test

ZnO, ZnO - Cu, ZnO - Mn, ZnO - CM ($60\ \mu\text{g}/\text{mL}$) were incubated separately with ST ($10^7\ \text{CFU}/\text{mL}$) at 37°C for a total of 4 h, followed by centrifugation at 5000 rpm for 5 min to precipitate the bacteria quickly. The supernatant was collected, and protein concentration was measured using the BCA protein assay kit (Beyotime, P0012). BCA standard method was used to calculate the concentration of protein in the supernatant overflow.

Cell viability

We utilized the CCK-8 assay kit (Beyotime, C0039) to assess the cytotoxicity of ZnO and ZnO-CM in RAW 246.7 cells as well as in intestinal epithelial cells. Briefly, 5×10^4 cells were seeded into 96-well plates. After 24 h, fresh medium containing varying concentrations of ZnO and ZnO-CM was added, and the cells were incubated for an additional 24 h. Subsequently, the medium was replaced with fresh medium, and $10\ \mu\text{L}$ of CCK-8 was added and incubated for 1 h (Six complex holes were set at each concentration). Absorbance was measured

at a wavelength of 450 nm. Cell viability was calculated according to the control group.

Salmonella infection in mice

C57BL/6 mice were obtained from Gempharmatech Co.Ltd. All aspects of animal daily care and experimental procedures were performed in accordance with the guidelines approved by the Animal Ethics Committee of Sichuan Agricultural University. (Permit Number: SICAU 2024-06-159). For the *in vivo* *Salmonella* infection experiment, 6-week-old C57BL/6 mice were used. Before infection, all mice were orally pre-fed with streptomycin (SM) at a dose of 25 mg/kg mouse for 48 h. Then, the mice were gavaged with $1.25 \times 10^8\ \text{CFU}/100\ \mu\text{L}$ of red fluorescent protein expression of *Salmonella* (ST-RFP, ATCC14028). Oral administration of ZnO-CM was continued for 4 days at doses of 25 mg/kg (Low) and 50 mg/kg (High), while the mice were transferred to Sterilized mouse culture cages to minimize re-colonization of the intestines from the environment. The control group was treated in parallel with 0.9% saline solution. The body weight of the mice was recorded daily throughout the entire testing period [23]. The intensity of the red fluorescent signal of *Salmonella* can be visually explored using in Multifunctional imaging system (UVP iBox Scientia, Analytik Jena, Germany). Additionally, colon length was measured, and distal colon tissue samples were collected for histology and western blot analysis. Details of the relevant antibodies are provided in Table S2.

Antimicrobial performance assay *in vivo*

Animals were euthanized and the small intestine and colon tissues were aseptically collected. Tissues of equal weight (10 mg) were homogenized in pre-cooled 1% sodium dodecyl sulfate (SDS) and serially diluted (10^1 to 10^5). The dilutions were then plated onto LB agar plates. After incubation at 37°C for 18 h, colonies were counted, and CFU values per milligram of tissue were calculated. Paraffin-embedded sections of small intestine/colon tissues fixed in 4% paraformaldehyde were deparaffinized. The nuclei were stained with DAPI, and the fluorescence intensity of ST-RFP was recorded using immunofluorescence.

Preliminary safety assessment

Mice from the infection groups at 24 h, 48 h, 7 days, and 14 days, as well as from the blank group, were euthanized. Blood was collected from the orbital venous plexus to assess routine blood parameters, as well as aspartate aminotransferase (AST) and alanine aminotransferase (ALT) levels. The major organs including the liver, kidney, spleen, lung, and heart were collected and placed in a $10\ \text{mL}$ solution of 4% paraformaldehyde for fixation, followed by paraffin embedding and Hematoxylin and Eosin

(H&E) staining to observe morphological changes in the organ tissues. Approximately 0.1 g of heart, liver, spleen, lung, and kidney tissues were transferred into 10 mL of concentrated nitric acid [24]. The samples were digested in a microwave digestion system at 180 °C. After digestion, the samples were cooled and then transferred to a volumetric flask to make up the volume to 10 mL. Finally, the samples were diluted 10 times with ultrapure water. Quantitative analysis of Cu, Mn, and Zn was carried out using Inductively Coupled Plasma Mass Spectrometry (ICP-MS). The content of the metals is expressed in nanograms of metal per gram of tissue material.

Statistical analysis

Each experimental group was subjected to at least three independent replicates, and the data are presented as mean \pm SD. The differences between multiple experimental groups were analyzed by one-way analysis of variance (ANOVA), and the statistical comparison between two groups employed the two-tailed, independent student-t test. The tests were regarded as statistically significant at $*p < 0.05$ (significant), $**p < 0.01$ (moderately significant), and $***p < 0.001$ (highly significant).

Results and discussion

Preparation and characterization of ZnO-CM

ZnO-CM were synthesized using a hydrothermal one-pot method [25, 26]. As depicted in Fig. 1A, B, S2 and S3, the electron micrographs reveal that the synthesized ZnO-CM exhibits a spherical morphology, with particles

uniformly distributed and a size of approximately 430 nm (Fig. 1F). Notably, there is no significant difference in morphology or particle size when compared to undoped ZnO, suggesting that the incorporation of Cu and Mn does not affect the structural characteristics of the nanospheres. TEM images display a characteristic ZnO lattice fringe with a (100) crystal spacing of 0.28 nm, indicating that Cu and Mn doping does not alter the crystalline structure (Fig. 1C, D). HAADF-STEM images and EDX elemental mapping (Fig. 1E) demonstrate that Zn, O, Cu, and Mn are uniformly distributed throughout the entire crystal lattice of ZnO-CM, further confirming the successful synthesis of the ZnO-CM nanospheres.

Zeta potentials for ZnO and ZnO-CM were measured to be -19 mV and -4.63 mV, respectively. The significant increase in the zeta potential of ZnO-CM, compared to the single doping of Cu or Mn (Fig. 2A), suggesting that elemental co-doping influences the zeta potential. ICP-MS analysis (Table S1) determined that the contents of Cu and Mn in the ZnO-CM nanospheres are 4.7 wt % and 7.6 wt %, respectively. To analyze the crystal structure and surface chemical environments of ZnO-CM nanospheres, XRD and XPS were performed. As shown in Fig. 2B and Fig. S4, the ZnO samples before and after Cu/Mn doping had a typical wurtzite-type phase (PDF No. 79-2205) [27]. No other characteristic peaks assigned to metallic Cu, Mn or oxide phases appeared in ZnO-CM, illustrating that Cu and Mn were doped into the ZnO lattice without changing the ZnO phase structure [28]. The XPS results show that, compared to undoped

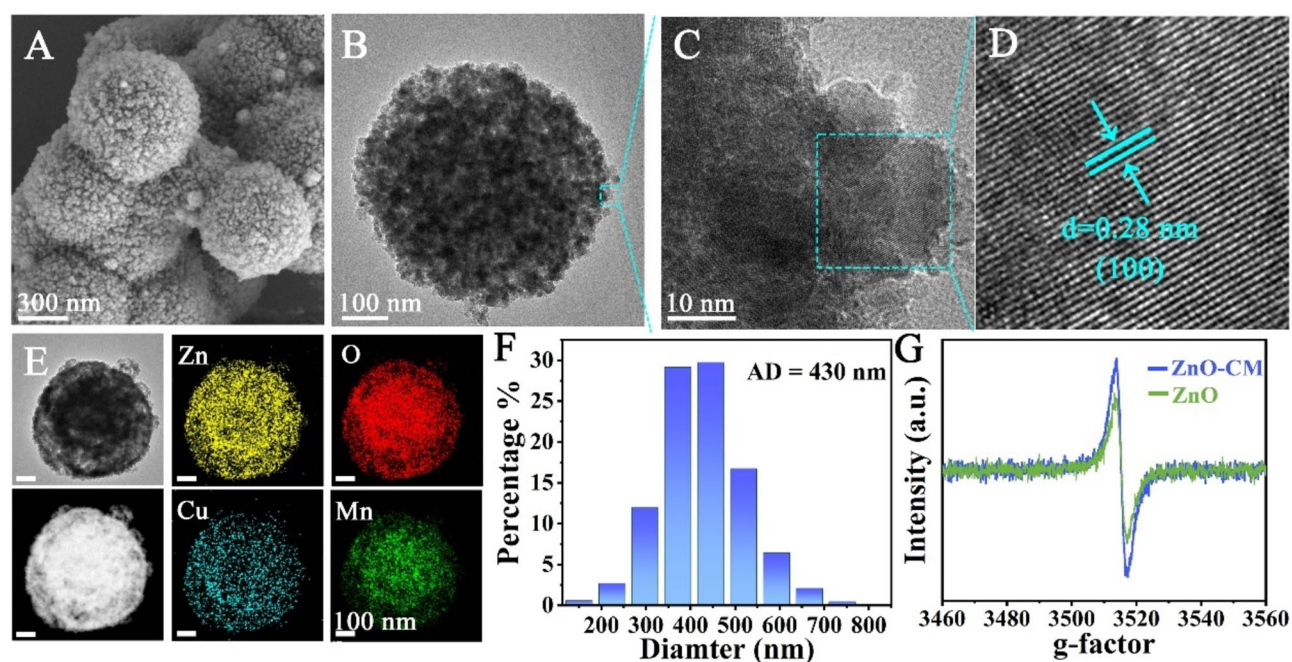


Fig. 1 Characterization of ZnO-CM. (A) SEM, (B, C) TEM and (D) lattice constant of ZnO-CM. (E) Elemental mapping of ZnO-CM. (F) size distribution of the ZnO-CM nanosphere. (G) EPR spectra of ZnO and ZnO-CM nanospheres

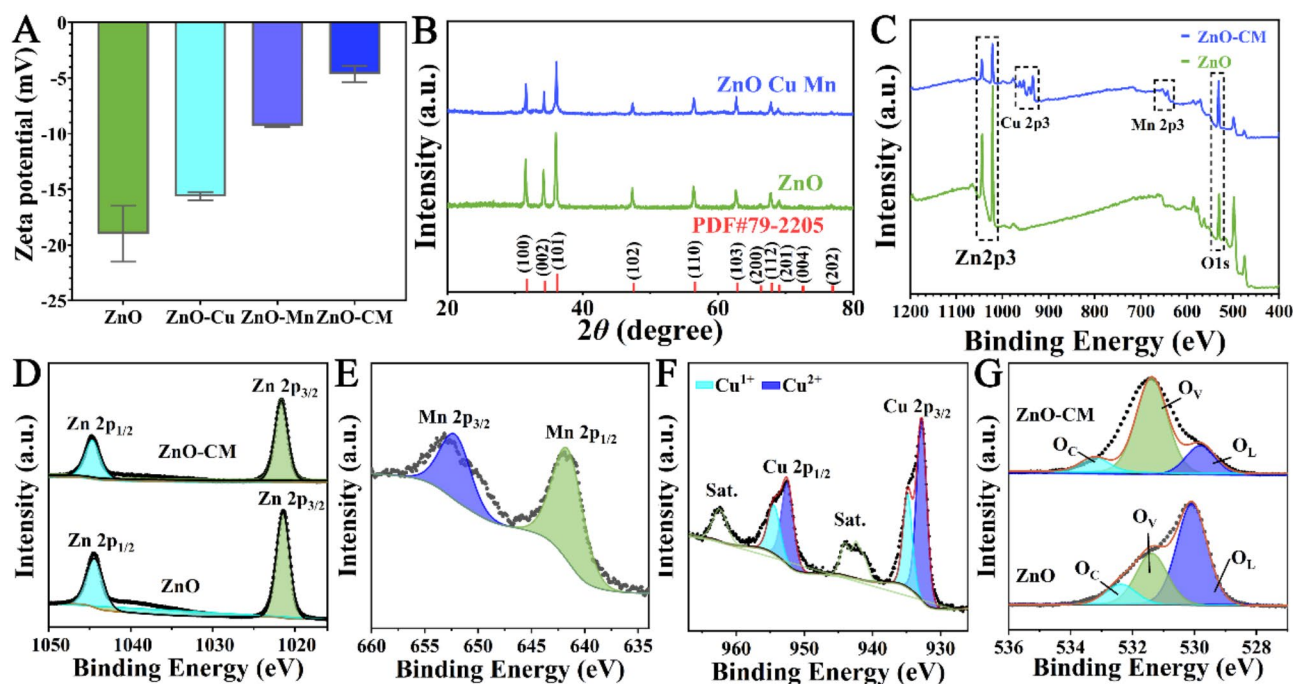


Fig. 2 Characterization of ZnO-CM. (A) Zeta Potential of ZnO, ZnO-Cu, ZnO-Mn and ZnO-CM. (B) XRD of ZnO and ZnO-CM (PDF#79-2205) (C) Survey XPS spectra of ZnO and ZnO-CM nanospheres. (D-G) XPS of ZnO-CM

ZnO, ZnO-CM exhibits signal of Cu and Mn in addition to Zn and O elements, further confirming the successful doping of Cu and Mn (Fig. 2C). For the ZnO, the XPS spectrum of Zn 2p exhibits two peaks located at 1021.68 and 1044.88 eV, belonging to the 2p_{1/2} and 2p_{3/2} of Zn²⁺, respectively [29]. After doping with Cu and Mn, the peaks intensities decrease and shift slightly to higher binding energy, suggesting that the electron density of Zn decreases owing to the doping of Cu and Mn [30] (Fig. 2D). The high-resolution XPS spectrum of Mn 2p exhibits two separated peaks at 653.28 and 641.99 eV, which can be assigned to Mn 2p_{3/2} and Mn 2p_{1/2} of Mn²⁺ (Fig. 2E), respectively. The Cu 2p spectrum contains four dominant peaks, with the peaks at 932.79 and 952.69 eV corresponding to Cu 2p_{3/2} and Cu 2p_{1/2}, respectively. Other peaks at 962.38 and 944.08 eV are assigned to satellites (labeled as “Sat.”). Notably, the peaks converge at 933.12, 952.66, 934.40, and 954.40 eV, signifying the binding energies of Cu(I) and Cu(II) and indicating the coexistence of both Cu(I) and Cu(II) species on the surface of ZnO-CM (Fig. 2F) [31]. The O1s spectrum are deconvoluted into three peaks (Fig. 2G), which are fitted by constituents corresponding to the lattice oxygen (O_L), vacant oxygen (O_V), and surface oxygen (O_C). The intensity of vacant oxygen significantly increased, revealing that Cu and Mn doping induced the generation of a great number of oxygen vacancies. In addition, this increase in oxygen vacancy concentration was further verified by electron paramagnetic resonance

(EPR) analysis. As shown in Fig. 1G, ZnO-CM displays an intense signal at g=2.037, corresponding to the electrons trapped on the oxygen vacancy, as compared with the EPR signal detected for undoped ZnO [17].

Evaluation of enzyme-like activity

We systematically compared the enzymatic activity in various doped ZnO (Fig. 3A), specifically assessing the peroxidase-like (POD-like) activity of ZnO-CM with 3,3',5,5'-tetramethylbenzidine (TMB) as an indicator. TMB undergoes a color change from colorless to blue oxTMB, demonstrating a UV-vis absorption peak at 652 nm. ZnO-CM and single-doped ZnO, namely ZnO-Cu and ZnO-Mn, both oxidize TMB, confirming their POD-like activity, and the catalytic activity of ZnO-CM is significantly higher than that of the single-doped variants (Fig. 3B). Electron spin resonance (ESR) measurements were performed to prove the generation of OH under acidic conditions (Fig. 3C). It is obvious that the quartet characteristic DMPO-OH signal with an intensity ratio of 1:2:2:1 appears in both single- and co-doped ZnO. The signal intensity for ZnO-CM is significantly higher than that of ZnO doped only with Cu or Mn, indicating that more OH species were produced for ZnO-CM. The pH exploration results showed that the blue oxTMB can only be observed at pH=3-6.5, whereas no color change is observed at pH=7 and 8, revealing that the POD-like activity of ZnO-CM only occurred in acidic conditions (Fig. 3D). Thus, ZnO-CM can generate OH for

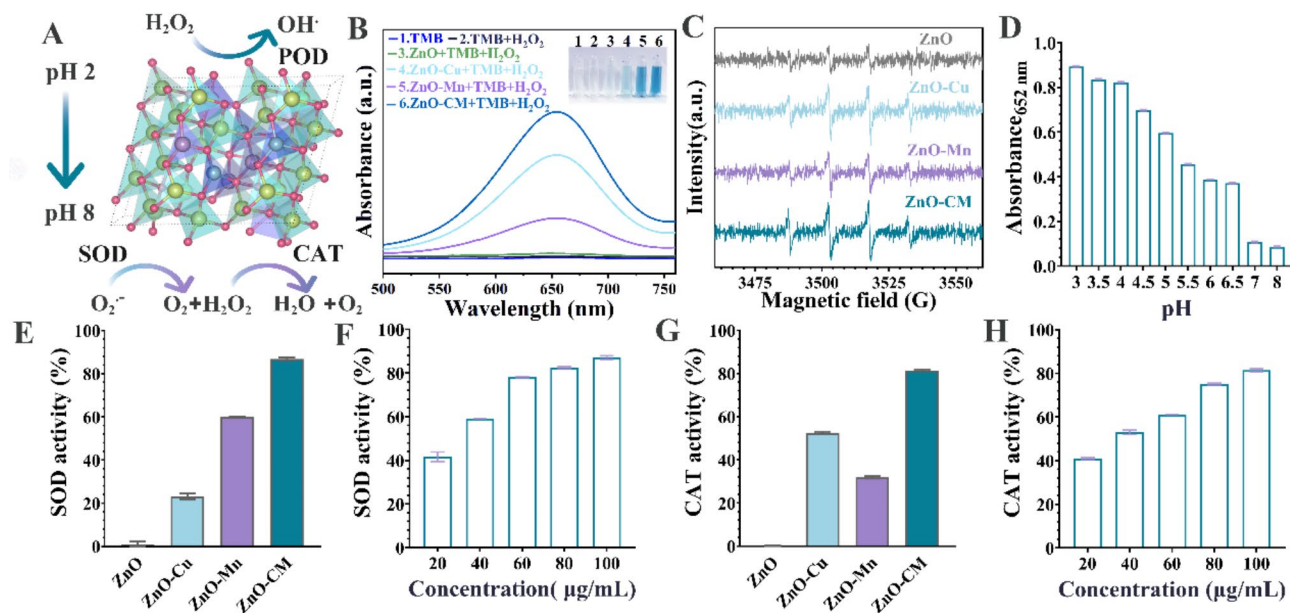


Fig. 3 Detection of enzyme-like activity of ZnO-CM. **(A)** Simulation diagram illustrating the enzyme activity reaction of ZnO-CM. **(B)** Test results for CAT enzyme activity. **(C)** ESR spin resonance spectrum with a pH of 3. **(D)** Oxidase enzyme activity under varying pH conditions. **(E)** Comparison of SOD enzyme activity at a concentration of 100 $\mu\text{g}/\text{ml}$ of ZnO and different doped ZnO variants. **(F)** SOD enzyme activity test conducted under different concentrations of ZnO-CM. **(G)** CAT enzyme activity measurements for 100 $\mu\text{g}/\text{ml}$ of ZnO and various doped ZnO samples. **(H)** Determination of CAT enzyme activity at different concentrations of ZnO-CM

antibacterial action in the acidic foregut while preserving antioxidant functions in the physiological hindgut (pH 7–7.8). It is well known that SOD is the initial line of resistance against ROS in organisms due to its ability to decompose $\text{O}_2^{\cdot-}$ [19]. We also evaluated the reactive oxygen species (ROS) scavenging activity of ZnO-CM under neutral conditions using nitrotetrazolium blue chloride (NBT) [32]. ZnO-Mn and ZnO-CM exhibit elimination ratios of approximately 60% and 86.8%, respectively. ZnO-CM demonstrate concentration-dependent superoxide dismutase (SOD)-like activity, reaching about 87% elimination at 100 $\mu\text{g mL}^{-1}$. Additionally, ZnO-CM shows excellent catalase (CAT)-like activity, being 1.55-fold and 2.56-fold higher than ZnO-Cu and ZnO-Mn, respectively, achieving approximately 81.43% H_2O_2 removal rate at the same concentration (Fig. 3E-H).

Theoretical calculations were conducted to elucidate the reaction mechanisms of SOD- and CAT-like activities in Cu/Mn single- or co-doped ZnO. The SOD-like pathway for ZnO-CM (Fig. 4A) and ZnO-Mn (Fig. S5) involves two key reactions: reduction and oxidation. In the reduction phase, OOH (a form of $\text{O}_2^{\cdot-}$ in water) [33] is absorbed to form $^*\text{OOH}$, which captures a proton from H_2O , yielding $^*\text{OH}-\text{H}_2\text{O}_2$ and releasing H_2O_2 . In the oxidation phase, the remaining $^*\text{OH}$ oxidizes an additional OOH free radical to form $^*\text{H}_2\text{O}-\text{O}_2$, followed by the release of O_2 . This SOD-like cycle consists of seven states, including two transition states (TS1/TS2); ZnO-CM exhibits significantly lower free energy

barriers (0.15 eV and 0.87 eV) than ZnO-Mn (0.75 eV and 1.65 eV) (Fig. 4B), indicating the preferred reactivity of ZnO-CM. For the CAT-like pathway, H_2O_2 is absorbed and decomposes into H_2O and the $^*\text{O}$ intermediate, which then combines with a second H_2O_2 , producing $^*\text{O}_2$ and releasing more water and O_2 (Fig. 4C). This catalytic cycle has five states, including two transition states, with ZnO-CM showing lower free energy barriers (0.96 eV and 0.72 eV) compared to ZnO-Cu (1.53 eV and 1.10 eV) (Fig. 4D). Collectively, these findings confirm that Cu/Mn co-doping effectively enhances the antioxidant capacity of ZnO, thereby enabling ZnO-CM to exhibit superior SOD-like and CAT-like activity.

Antibacterial study in vitro

Given the enzymatic properties of ZnO-CM, we examined its antibacterial activity in vitro. The antibacterial effect of ZnO-CM was further determined by plate counting method, as shown in Fig. 5A. It indicates that ZnO-CM exhibits the strongest bactericidal effect, significantly reducing bacterial viability at lower concentrations compared to ZnO, ZnO-Cu, and ZnO-Mn, and the inhibition rate increases with the concentration of ZnO-CM. Additionally, a significant reduction in colony count is observed, but there is still noticeable bacterial growth in the 30 $\mu\text{g}/\text{mL}$ treatment group. However, the colony count is extremely low, indicating a strong bactericidal effect in the 60 $\mu\text{g}/\text{mL}$ treatment group (Fig. 5A). The minimum bactericidal concentration (MBC) was

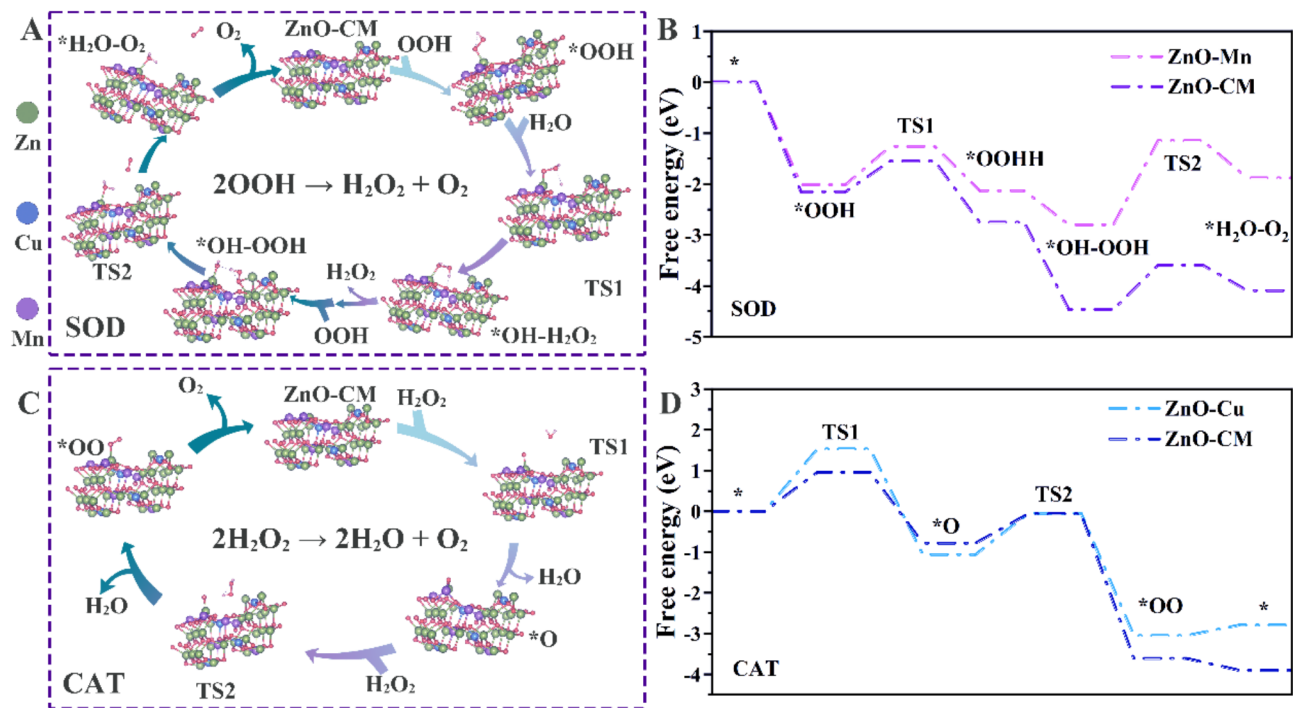


Fig. 4 Simulation of the mechanism of ZnO-CM (A) Simulation and calculation of SOD activity for ZnO-CM. (B) Comparison of energy barrier changes between ZnO-Mn and ZnO-CM. (C) Simulation of CAT enzyme activity for ZnO-CM and (D) Comparison of energy barrier changes between ZnO-Cu and ZnO-CM reactions

determined to be 125 $\mu\text{g}/\text{mL}$ for ZnO-CM. At a concentration of 1000 $\mu\text{g}/\text{mL}$, the antibacterial effect of ZnO-Cu is significantly enhanced, with almost complete elimination of bacteria, which may be due to the bactericidal effect of Cu ions. ZnO doped with Mn only demonstrates a slight bactericidal effect, and its bactericidal efficacy does not significantly increase with the concentration. However, ZnO doped with both Cu and Mn exhibits the best bactericidal effect at low concentrations, achieving a bactericidal efficiency of 98% at a concentration of 60 $\mu\text{g}/\text{mL}$ (Fig. 5A). Cu further enhances the bacteriostatic effect [34, 35]. Under the influence of nanomaterials, bacterial membranes may experience damage or pore formation, after co-incubation with *Salmonella* for 18 h, ZnO-CM treatment significantly caused membrane damage and structural alterations in the bacteria (Fig. 5D). When membrane damage reaches a certain threshold, it causes substantial loss of cellular contents, ultimately resulting in bacterial death. Among these cellular contents, proteins can serve as indicators [36]. Therefore, by utilizing the BCA method, we can directly observe the quantity of protein leaked into the external environment under different treatments (Control, ZnO, ZnO-Cu, ZnO-Mn, ZnO-CM) at the same dosage, where the protein leakage measured in the ZnO-CM treatment group is 0.44 mg/L, which outperform the blank and ZnO-only groups (Fig. 5B). Additionally, the bacterial growth curve reveals that at 60 $\mu\text{g}/\text{mL}$, the bacterial growth in

the ZnO-CM treatment group ceases over time (Fig. 5C). As a broad-spectrum antibacterial agent [37], ZnO disrupts bacterial membranes and leads to protein leakage [38, 39], while the peroxidase activity of ZnO-CM may produce hydroxyl radicals under certain conditions (pH 3-6.5) to achieve synergistic bactericidal effect [39].

Preliminary safety assessment

To ensure the practical applicability of ZnO-CM, it is essential to thoroughly assess its biological toxicity. Initially, the cytotoxicity of ZnO-CM was evaluated in both RAW 264.7 and MECE cells. The results from the CCK-8 assay indicated that there was minimal cell death in MECE cells at a ZnO concentration of 20 $\mu\text{g}/\text{mL}$. At a concentration of 40 $\mu\text{g}/\text{mL}$, cell viability was 80.79%, while ZnO-CM exhibited a viability of 82.33%. However, when the concentration increased to 80 $\mu\text{g}/\text{mL}$, cell viability dropped to 46.43%, and the viability for ZnO-CM fell to 62.85%. These findings suggest that ZnO-CM exhibits lower cytotoxicity compared to ZnO at concentrations of up to 80 $\mu\text{g}/\text{mL}$ (Fig. 6A). Similar results are observed in RAW 264.7 cells treated with ZnO-CM (Fig. 6B). Subsequently, the in vivo biocompatibility of ZnO-CM was thoroughly evaluated in 8-week-old BALB/c mice. After 14 days of continuous ZnO-CM administration, the body weight of the mice continues to increase, with no significant differences observed between the groups (Fig. 6C). Pathological

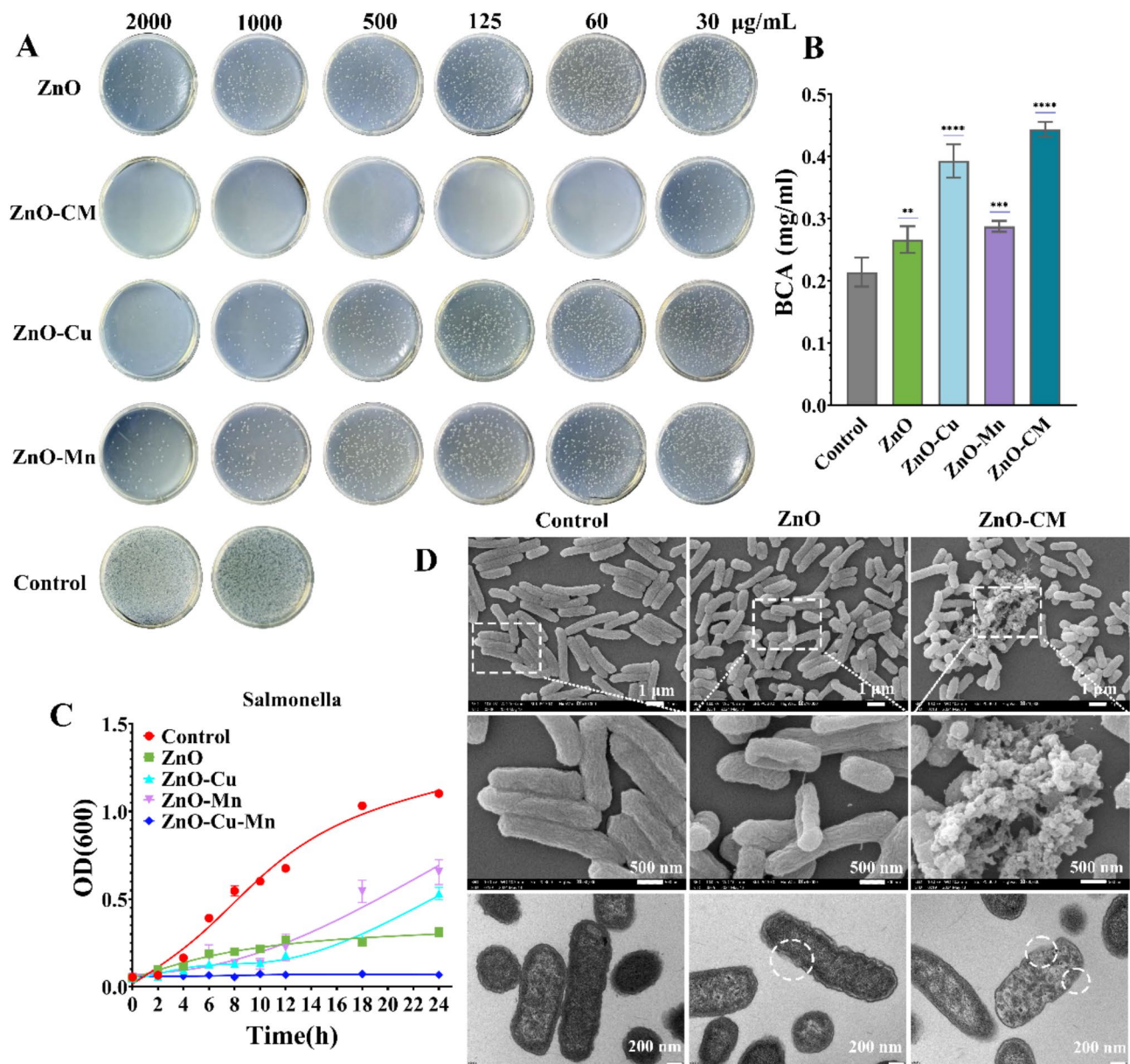


Fig. 5 Antibacterial effects of ZnO and different doped ZnO *in vitro*. **(A)** MBC coating test results for ZnO, ZnO-Cu, ZnO-Mn, and ZnO-CM. **(B)** Using the BCA method, protein leakage from bacteria was measured following 18 h of incubation with ZnO, ZnO-Cu, ZnO-Mn, and ZnO-CM at 60 µg/ml. **(C)** Bacterial growth curves for the treatments with 60 µg/ml of ZnO, ZnO-Cu, ZnO-Mn, and ZnO-CM. **(D)** SEM images and TEM images of bacteria after 1 h of incubation with 60 µg/ml of ZnO and ZnO-CM. ***Note:** Statistical significance is indicated as follows: * $p < 0.05$, ** $p < 0.01$, *** $p < 0.001$

examination reveals no necrosis, congestion, or hemorrhage in the heart, liver, spleen, lung, or kidney in any of the groups (Fig. 6D). Whole blood analysis results (RBC, HGB, HCT, MCV, MCH, WBC and PLT) show no differences between the ZnO-CM treated group and the control group (Fig. 6E-L). Furthermore, serum biochemical analysis indicates that the liver function parameters (AST and ALT) in the ZnO-CM treatment group are similar to those in the control group (Fig. 6M, N), demonstrating its good biocompatibility with the liver.

Given the concerns regarding elemental accumulation in visceral tissues, a common issue associated with metal-based nanocatalysts, we performed ICP-MS testing on the hearts, livers, spleens, lungs, and kidneys of mice at different time points to investigate the accumulation of metal elements. The results reveal no significant differences in the levels of Cu and Mn across the various metabolic organs as dosing duration increased (Fig. 6O-S). However, Zn exhibited slight accumulation in the spleen after administration for a duration of 48 h to 14 days compared to the control group. Interestingly, instead

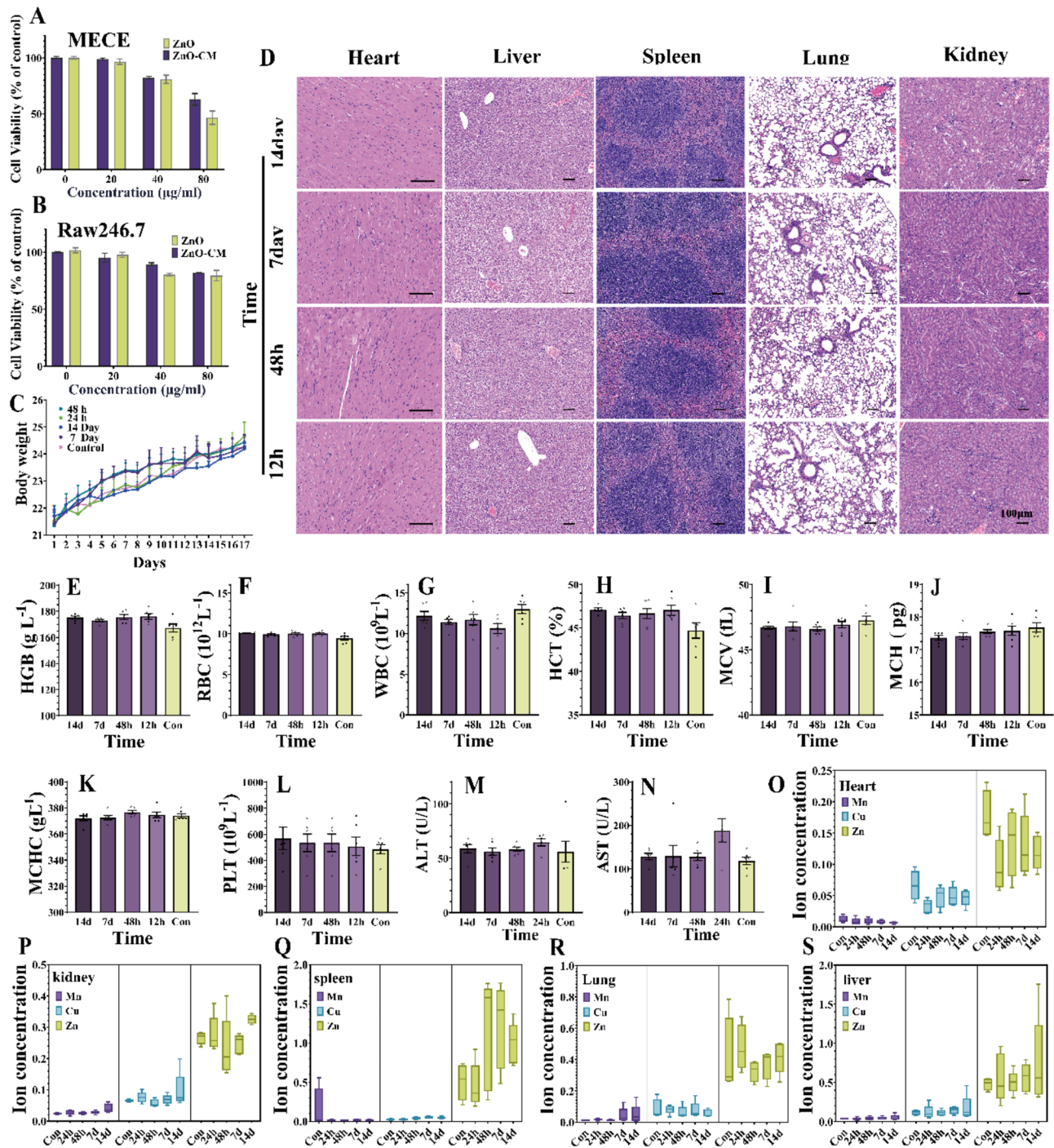


Fig. 6 preliminary safety assessment. **(A)** ZnO and ZnO-CM cytotoxicity of intestinal epithelial cells. **(B)** Cytotoxicity of ZnO and ZnO-CM on RAW 264.7 cells. **(C)** mice weight figure. **(D)** 24 h, 48 h after the treatment, 7 days and 14 days on heart, liver, spleen, lung and kidney tissue histological evaluation. **(E-L)** routine blood levels of mice. **(M,N)** in mice serum alanine aminotransferase (ALT) and aspartate aminotransferase (AST) levels. **(O-S)** nanometer material of Cu, Mn, Zn distribution in organs

of a continuous increase in accumulated Zn over time, a decreasing trend was observed. No significant changes were noted in other organs, suggesting that ZnO-CM is cleared relatively quickly in vivo with low potential for long-term toxicity.

Antibacterial and anti-inflammation evaluation in vivo

We then investigated the antibacterial and anti-enteritis effects of ZnO-CM in mice infected with *Salmonella* (Fig. 7A). The Model group exhibits a 45% mortality rate within two days post-infection, while the ZnO group

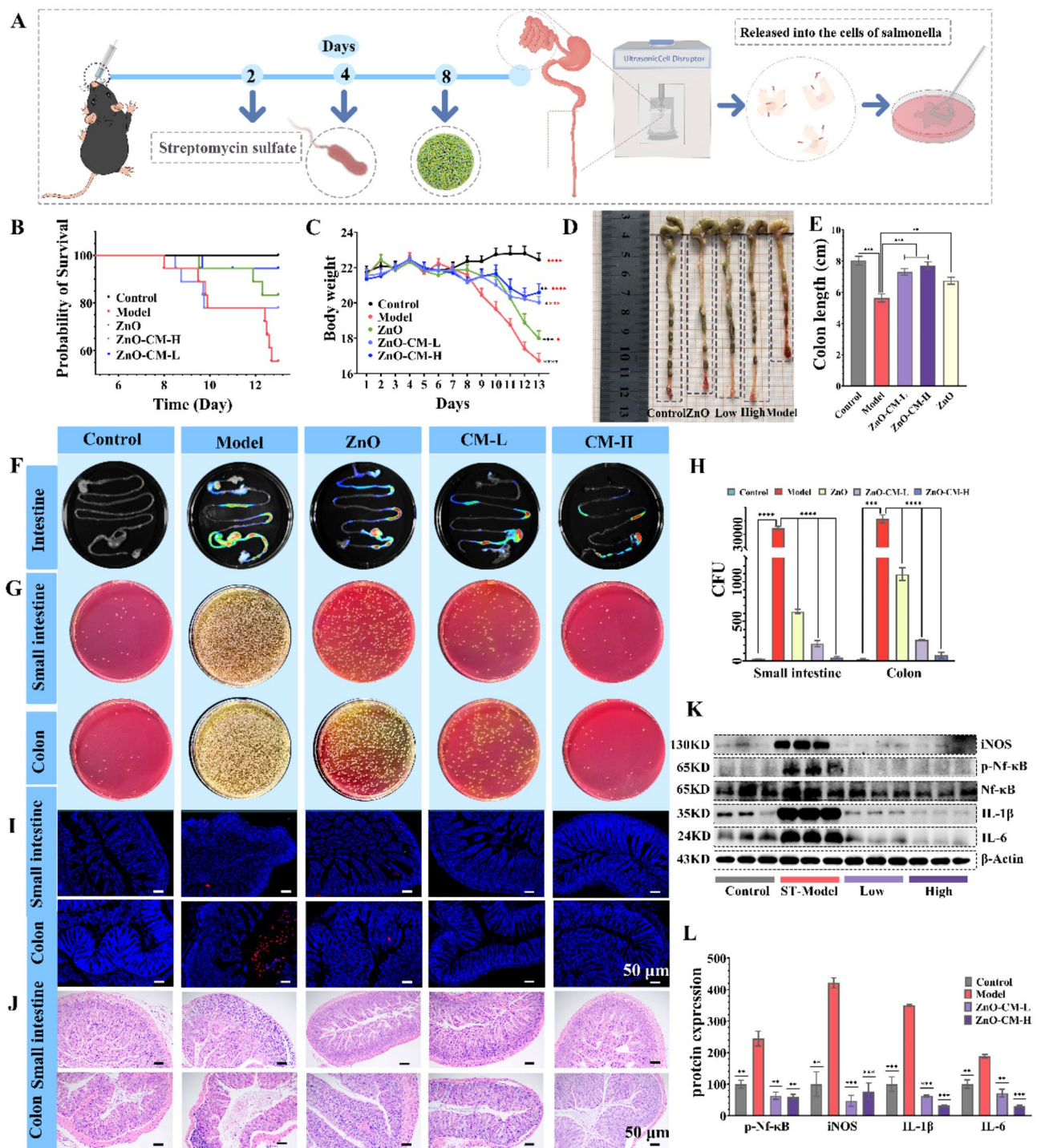


Fig. 7 The antibacterial and anti-inflammatory effect of ZnO-CM in vivo in a *Salmonella*-infected enteritis model. Groups are divided into Control, Model, ZnO (50 mg/kg), ZnO-CM-L (25 mg/kg), and ZnO-CM-H (50 mg/kg). **(A)** Schematic of the mouse model establishment and subsequent testing of antibacterial effects in the colon and small intestine. **(B)** Mortality curves ($n=20$). **(C)** curves of body weight in mice. **(D)** Comparison of colon length after treatment of *Salmonella* infection. **(E)** Quantification of colon length. **(F)** ex vivo visceral imaging showing bacterial concentration and distribution. **(G,H)** groups of small intestine and colon bacteria smear photos and quantification after treatment. **(I)** immunofluorescence observations tissue section distribution of bacteria. **(J)** Hematoxylin-eosin (HE) staining of tissue sections of the small intestine and colon. **(K,L)** expression levels of inflammation-related proteins. $n=10$, * $p<0.05$, ** $p<0.01$, *** $p<0.001$

shows a reduced mortality rate of 10%. Importantly, mice treated with either dose of ZnO-CM experiences no additional deaths over four days (Fig. 7B). *Salmonella* infection results in a 30% reduction in body weight, which is partially alleviated by ZnO (20% reduction) and significantly improved by ZnO-CM (5% reduction) (Fig. 7C). Furthermore, *Salmonella* infection leads to significant colon shortening, indicative of colitis, which is notably alleviated by ZnO-CM treatment (Fig. 7D and E). To evaluate *Salmonella* distribution and the bactericidal efficacy of ZnO-CM, we infected mice with ST-RFP. In vivo imaging reveals *Salmonella* accumulation in the cecum and colon (Fig. 7F). ZnO treatment reduces *Salmonella* numbers by 98% in the small intestine and 96% in the colon, whereas ZnO-CM achieves over a 99% reduction, with the ZnO-CM-H group demonstrating nearly complete eradication (Fig. 7G and H). Immunofluorescence confirmed ZnO-CM's in vivo effectiveness in killing *Salmonella*, paralleling in vitro results (Fig. 7I). Hematoxylin and eosin (HE) staining demonstrates that both ZnO and ZnO-CM reduce *Salmonella*-induced colon damage, with ZnO-CM exhibiting a stronger protective effect (Fig. 7J). A similar protective effect is observed in the small intestine (Fig. 7J). *Salmonella* infection caused inflammation and cell death, compromising the intestinal barrier function, as evidenced by decreased levels of tight junction proteins occludin and claudin-1, which were restored by ZnO-CM treatment (Fig. S6). Infection activated NF- κ B phosphorylation, increasing expression of pro-inflammatory cytokines IL-1 β and IL-6, but ZnO-CM significantly reduced these cytokines (Fig. 7K and L). *Salmonella* infection also upregulated iNOS expression [40], while ZnO-CM reduced it, indicating its role in inhibiting M1 macrophage polarization and thereby relieving *Salmonella*-induced colitis (Fig. 6F-I) [41]. Therefore, ZnO-CM effectively reduces *Salmonella*-induced colon damage, weight loss, and mortality in mice (Fig. 7B-E).

Conclusion

In summary, we successfully synthesized a Cu/Mn co-doped ZnO tandem nanozyme (ZnO-CM) with exceptional POD, SOD, and CAT-like activities using a straightforward doping engineering approach and systematically investigated its effects on the progression of *Salmonella* infection and the induced colitis. ZnO-CM demonstrated a dual-action mechanism: under acidic conditions, its POD-like activity disrupted bacterial biofilms and generated hydroxyl radicals (\bullet OH), exhibiting potent antibacterial effects that inhibited *Salmonella* proliferation and reduced intestinal damage. In neutral environments, its SOD and CAT-like activities effectively scavenged excess ROS, enhancing antioxidant capacity and mitigating oxidative stress, thereby alleviating

Salmonella-induced colitis. This dual functionality not only offers a novel therapeutic approach for *Salmonella* infections but also presents a promising alternative to traditional antibiotics. Moreover, the facile production of this multifunctional nanozyme provides valuable insights for nanozyme design and optimization, with potential applications in treating other bacterial infections and inflammatory diseases. Future research should focus on evaluating the strategy's efficacy, safety, and potential side effects across various pathogens and disease models, as well as assessing its clinical applicability through dose optimization, administration routes, and synergistic effects with existing therapies. Multidisciplinary collaboration and long-term studies are essential to fully realize the potential of this strategy in addressing antibiotic resistance and bacterial infections.

Abbreviations

ALT	Alanine aminotransferase
AST	Aspartate aminotransferase
CAT	Catalase
CFU	Colony forming unit
DFT	Density functional theory
EDS	Energy-dispersive spectrometry
EPR	Electron paramagnetic resonance
ESR	Electron spin resonance
GGA-PBE	Generalized gradient approximation of perdew-burke-ernzerhof
GRAS	Generally recognized as safe
HCT	Hematocrit
HGB	Hemoglobin
ICP-MS	Inductively coupled plasma mass spectrometry
MBC	Minimum bactericidal concentration
MCH	Mean corpuscular hemoglobin
MCV	Mean corpuscular volume
OH	Inducing hydroxyl radicals
NBT	The nitroblue tetrazolium
NF- κ B	Nuclear factor kappa-B
O ₂ ⁻	Superoxide anions
OAm	Oleylamine
O _c	Surface oxygen
O _L	Lattice oxygen
O _v	Vacant oxygen
PAW	The projector augmented-wave
PLT	Platelet
POD	Peroxidase
RBC	Red blood cell count
SEM	Scanning electron microscopy
SOD	Superoxide dismutase
ST-RFP	Red fluorescent protein expression of <i>Salmonella</i>
TEM	Transmission electron microscope
TMB	3,3',5,5'-tetramethylbenzidine
VASP	Vienna ab Initio simulation package
WBC	White blood cell
XPS	X-ray photoelectron spectroscopy
XRD	X-ray diffraction
ZnO-CM	Cu/Mn-co-doped ZnO

Supplementary Information

The online version contains supplementary material available at <https://doi.org/10.1186/s12951-025-03283-4>.

Supplementary Material 1

Acknowledgements

We express our sincere gratitude to Sichuan Chelota Biotechnology Group Co., Ltd. for providing the pilot production facility that contributed to this study.

Author contributions

Aimin Wu and Chen Liang contributed equally to this work. Aimin Wu and Chen Liang: conception, methodology, material preparation, experiment conduction, data presentation, analysis, writing. Wenshuang Chen, Changfang Lu, Junzhou Chen and Bing Wu: experiment conduction, methodology, data presentation, software. Daiwen Chen, LiHe and Xianxiang Wang: revision, edit, supervision, conception, methodology.

Funding

This work was supported by the National Natural Science Foundation of Sichuan Province (Grant No. 24NSFSC0279) and the Joint Funds of the National Natural Science Foundation of China (Grant No. U22A20513).

Data availability

No datasets were generated or analysed during the current study.

Declarations

Ethics approval and consent to participate

Ethics approval Animal protocols were approved by the Animal Experimental Committee of Sichuan Agricultural University, (Permit Number: SICAU 2024-06-159).

Consent for publication

All authors of this study agreed to publish.

Competing interests

The authors declare no competing interests.

Received: 22 January 2025 / Accepted: 28 February 2025

Published online: 20 March 2025

References

- Li H, Wu Y, Feng D, Jiang Q, Li S, Rong J, Zhong L, Methner U, Baxter L, Ott S, et al. Centralized industrialization of pork in Europe and America contributes to the global spread of *Salmonella enterica*. *Nat Food*. 2024;5:00968.
- Upadhyay A, Pal D, Kumar A. Interrogating *Salmonella* Typhi biofilm formation and dynamics to understand antimicrobial resistance. *Life Sci*. 2024;339:122418.
- Li ST, He YS, Mann DA, Deng XY. Global spread of *Salmonella enteritidis* via centralized sourcing and international trade of poultry breeding stocks. *Nat Commun*. 2021;12:5109.
- Ellermeier JR, Schlauch JM. Adaptation to the host environment: regulation of the SPI1 type III secretion system in *Salmonella enterica* serovar typhimurium. *Curr Opin Microbiol*. 2007;10:24–9.
- Gal-Mor O. Persistent infection and Long-Term carriage of typhoidal and nontyphoidal *Salmonellae*. *Clin Microbiol Rev*. 2019;32:00088–00018.
- Gao C, Kwong CHT, Tang M, Liu J, Kam H, Li S, Lee SMY, Fan C, Yu H-Z, Wang R. A bacterially engineered macrophage sponge as a neutralization decoy to treat bacterial infection. *Matter*. 2023;6:3889–911.
- Sellin ME, Müller AA, Felmy B, Dolowischkiak T, Diard M, Tardivel A, Maslowski KM, Hardt WD. Epithelium-Intrinsic NAIP/NLRC4 inflammasome drives infected enterocyte expulsion to restrict *Salmonella* replication in the intestinal mucosa. *Cell Host Microbe*. 2014;16:237–48.
- Jiang LY, Wang PS, Song XR, Zhang H, Ma SS, Wang JT, Li WW, Lv RX, Liu XQ, Ma S, et al. *Salmonella* Typhimurium reprograms macrophage metabolism via T3SS effector SopE2 to promote intracellular replication and virulence. *Nat Commun*. 2021;12:879.
- Xu S, He Y, Lin LH, Chen P, Chen MH, Zhang SH. The emerging role of ferroptosis in intestinal disease. *Cell Death Dis*. 2021;12:289.
- Ramanan D, Cadwell K. Intrinsic defense mechanisms of the intestinal epithelium. *Cell Host Microbe*. 2016;19:434–41.
- Wang YY, Wu CM, Gao JC, Du XD, Chen XY, Zhang M. Host metabolic shift during systemic *Salmonella* infection revealed by comparative proteomics. *Emerg Microbes Infect*. 2021;10:1849–61.
- Hurley JC. Antibiotic-Induced release of endotoxin: A reappraisal. *Clin Infect Dis*. 1992;15:840–54.
- Mendes CR, Dilarrri G, Forsan CF, Sapata VMR, Lopes PRM, de Moraes PB, Montagnolli RN, Ferreira H, Bidoia ED. Antibacterial action and target mechanisms of zinc oxide nanoparticles against bacterial pathogens. *Sci Rep*. 2022;12:2658.
- Zhou Z, Mei X, Hu K, Ma M, Zhang Y. Nanohybrid double network hydrogels based on a platinum nanozyme composite for antimicrobial and diabetic wound healing. *ACS Appl Mater Interfaces*. 2023;15:17612–26.
- Ma X, Lang J, Chen P, Tang W, Shindler S, Yang R. A cascade nanozyme with antimicrobial effects against nontypeable *Chlamydia pneumoniae*. *Nanoscale*. 2023;15:1014–23.
- Mohammad M, Ahmadpoor F, Shojasoadati SA. Mussel-Inspired magnetic nanoflowers as an effective nanozyme and antimicrobial agent for biosensing and catalytic reduction of organic dyes. *ACS Omega*. 2020;5:18766–77.
- Wang DD, Wu HH, Wang CL, Gu L, Chen HZ, Jana D, Feng LL, Liu JW, Wang XY, Xu PP, et al. Self-assembled single-site nanozyme for tumor-specific amplified cascade enzymatic therapy. *Angew Chem Int Ed*. 2021;60:3001–7.
- Sun ZD, Shao YZ, Yan KH, Yao TZ, Liu LL, Sun FF, Wu JR, Huang YP. The link between trace metal elements and glucose metabolism: evidence from zinc, copper, iron, and manganese-mediated metabolic regulation. *Metabolites*. 2023;13:1048.
- Huang F, Lu X, Kuai L, Ru Y, Jiang J, Song J, Chen S, Mao L, Li Y, Li B, et al. Dual-site biomimetic Cu/Zn-MOF for atopic dermatitis catalytic therapy via suppressing FcγR-Mediated phagocytosis. *J Am Chem Soc*. 2024;146:3186–99.
- Joseph J, Ametepi ES, Haribabu N, Agbayani G, Krishnan L, Blais A, Sad S. Inhibition of ROS and upregulation of inflammatory cytokines by FoxO3a promotes survival against *Salmonella typhimurium*. *Nat Commun*. 2016;7:12748.
- Kwon K, Jung J, Sahu A, Tae G. Nanoreactor for cascade reaction between SOD and CAT and its tissue regeneration effect. *J Controlled Release*. 2022;344:160–72.
- Wen H, Li L, Ge X, Fei Y, Li Y, Li M, Xiao W, Luo Z. Hydrogel-based artificial mucosa restores local immune and microbial homeostasis for treating ulcerative colitis. *Adv Funct Mater*. 2023;33:2212566.
- Bakkeren E, Huisman JS, Fattinger SA, Hausmann A, Furter M, Egli A, Slack E, Sellin ME, Bonhoeffer S, Regoes RR, et al. *Salmonella* persists promote the spread of antibiotic resistance plasmids in the gut. *Nature*. 2019;573:276.
- Mumtaz S, Ali S, Tahir HM, Mumtaz S, Mughal TA, Kazmi SAR, Hassan A, Summer M, Zulfiqar A, Kazmi S. Biological applications of biogenic silk fibroin-chitosan blend zinc oxide nanoparticles. *Polym Bull*. 2024;81:2933–56.
- Tian BS, Tian RX, Liu SH, Wang Y, Gai SL, Xie Y, Yang D, He F, Yang PP, Lin J. Doping engineering to modulate lattice and electronic structure for enhanced piezocatalytic therapy and ferroptosis. *Adv Mater*. 2023;35:2304262.
- Liang W, Cheng J, Zhang J, Xiong Q, Jin M, Zhao J. pH-responsive on-demand alkaloids release from core-shell ZnO@ZIF-8 nanosphere for synergistic control of bacterial wilt disease. *ACS Nano*. 2022;16:2762–73.
- Ullah H, Iqbal A, Zakria M, Mahmood A. Structural and spectroscopic analysis of wurztzite (ZnO)_{1-x}(Sb₂O₃)_x composite semiconductor. *Prog Nat Sci: Mater Int*. 2015;25:131–6.
- Lindquist NC, Brolo AG. Ultra-High-Speed dynamics in Surface-Enhanced Raman scattering. *J Phys Chem C*. 2021;125:7523–32.
- Zhan S, Zhang H, Mi X, Zhao Y, Hu C, Lyu L. Efficient Fenton-like process for pollutant removal in Electron-Rich/Poor reaction sites induced by surface oxygen vacancy over Cobalt-Zinc oxides. *Environ Sci Technol*. 2020;54:8333–43.
- Wen YY, Chen J, Gao X, Liu W, Che HA, Liu B, Ao YH. Two birds with one stone: Cobalt-doping induces to enhanced piezoelectric property and persulfate activation ability of ZnO nanorods for efficient water purification. *Nano Energy*. 2023;107:108173.
- Wang XZ, Wang H, Cheng JF, Li H, Wu XF, Zhang DH, Shi XH, Zhang JK, Han N, Chen YF. Initiative ROS generation of Cu-doped ZIF-8 for excellent antibacterial performance. *Chem Eng J*. 2023; 466.
- Liu Y, Cheng Y, Zhang H, Zhou M, Yu Y, Lin S, Jiang B, Zhao X, Miao L, Wei C-W, et al. Integrated cascade nanozyme catalyzes in vivo ROS scavenging for anti-inflammatory therapy. *Sci Adv*. 2020;6:2695.
- Gao WH, He JY, Chen L, Meng XQ, Ma YN, Cheng LL, Tu KS, Gao XF, Liu C, Zhang MZ, et al. Deciphering the catalytic mechanism of superoxide dismutase activity of carbon dot nanozyme. *Nat Commun*. 2023;14:160.
- Xu W, Hou C, Mao Y, Yang L, Tamaddon M, Zhang J, Qu X, Liu C, Su B, Lu X. Characteristics of novel Ti-10Mo-xCu alloy by powder metallurgy for potential biomedical implant applications. *Bioactive Mater*. 2020;5:659–66.

35. Zhang C, Chu G, Ruan Z, Tang N, Song C, Li Q, Zhou W, Jin J, Haick H, Chen Y, Cui D. Biomimetic Self-Assembling Metal-Organic architectures with Non-Iridescent structural coloration for synergetic antibacterial and osteogenic activity of implants. *ACS Nano*. 2022;16:16584–97.
36. Sharma K, Sharma M. A molecular machine disrupts bacterial membranes. *Nat Microbiol*. 2024;9:584–584.
37. Tahir H, Rashid F, Ali S, Summer M, Abaidullah R, Spectrophotometrically. Spectroscopically, microscopically and thermogravimetrically optimized TiO₂ and ZnO nanoparticles and their bactericidal, antioxidant and cytotoxic potential: A novel comparative approach. *J Fluoresc*. 2024;34:2019–33.
38. Chai Q, Wu Q, Liu T, Tan L, Fu C, Ren X, Yang Y, Meng X. Enhanced antibacterial activity of silica nanorattles with ZnO combination nanoparticles against methicillin-resistant *Staphylococcus aureus*. *Sci Bull*. 2017;62:1207–15.
39. Sirelkhatim A, Mahmud S, Seeni A, Kaus NHM, Ann LC, Bakhori SKM, Hasan H, Mohamad D. Review on zinc oxide nanoparticles: antibacterial activity and toxicity mechanism. *Nano-Micro Lett*. 2015;7:219–42.
40. Nairz M, Fritsche G, Crouch M-LV, Barton HC, Fang FC, Weiss G. Slc11a1 limits intracellular growth of *Salmonella enterica* Sv. Typhimurium by promoting macrophage immune effector functions and impairing bacterial iron acquisition. *Cell Microbiol*. 2009;11:1365–81.
41. Zou Q, Han S, Liang J, Yan G, Wang Q, Wang Y, Zhang Z, Hu J, Li J, Yuan T, Liu Z. Alleviating effect of vagus nerve cutting in *Salmonella*-induced gut infections and anxiety-like behavior via enhancing microbiota-derived GABA. *Brain Behav Immun*. 2024;119:607–20.

Publisher's note

Springer Nature remains neutral with regard to jurisdictional claims in published maps and institutional affiliations.